Structural and photoelectrochemical properties of SrTaO2N oxynitride thin films deposited by reactive magnetron sputtering

Claire Le Paven-Thivet, A. Ziani, Florent Marlec, Laurent Le Gendre, Franck Tessier, Mohamad Haydoura, Ratiba Benzerga, François Cheviré, K. Takanabe, Ala Sharaiha

Structural and photoelectrochemical properties of $SrTaO_2N$ oxynitride thin films deposited by reactive magnetron sputtering

C. Le Paven[1*], A. Ziani[2], F. Marlec[1], L. Le Gendre[1], F. Tessier[3], M. Haydoura[1], R. Benzerga[1], F. Cheviré[3], K. Takanabe[2,4], A. Sharaiha[1]

[1] *Univ Rennes, CNRS, IETR UMR 6164, F-35000 Rennes, France.*

[2] *King Abdullah University of Science and Technology (KAUST), KAUST Catalysis Center (KCC) and Physical Sciences and Engineering Division (PSE), Thuwal, 23955 - 6900, Saudi Arabia.*

[3] *Univ Rennes, CNRS, ISCR UMR 6226, F-35000 Rennes, France.*

[4] *The University of Tokyo, 7-3-1 Hongo, Bunkyo-ku, Tokyo 113-8656, Japan.*

*claire.lepaven@univ-rennes1.fr

Highlights

- Sputtering deposition of $SrTaO_2N$ films on different types of substrates
- Films approach stoichiometry with a bandgap of 2.33 eV when substrate temperature increases to T_S = 800°C
- Different degrees of film crystallization, from weakly crystallized to fully c-axis oriented, were obtained
- Three limiting factors are identified: 1) low absorption coefficient; 2) short lifetimes of excited charge carriers; and 3) permittivity with moderate values
- Dual effects of a higher crystallinity and a greater absorbance for the thickest (600 nm) films.

Abstract

In this study, the influence of the degree of crystallization and thickness of films was correlated with the photoelectrochemical performance of $SrTaO_2N$ semiconductor films for O_2 evolution reaction under visible light irradiation. Oxynitride films were deposited on various substrates using the sputtering in Ar + N_2 reactive atmosphere from a home-made $SrTaO_2N$ target. Films

with stoichiometric composition were obtained at a high temperature (T_S = 800°C) with reduced bandgap. The different substrates led to diverse degrees of film crystallization, from weakly crystallized to fully c-axis oriented. The photoelectrochemical performance was improved by improving the film crystallinity and the thickness. For further improvement of the photoelectrochemical performance, the following three limiting factors are identified: 1) low absorption coefficient, especially in the visible domain from 500 to 600 nm; 2) short lifetimes of excited charge carriers; and 3) permittivity with only moderate values lower than 10 in the visible-light domain.

1. Introduction

Conversion of solar energy is attractive because it corresponds to an inexhaustible source of energy on a human scale. Over a year, the amount of solar energy absorbed by the Earth is 3,850 ZJ (ZJ, 10^{21} Joules) and the human energy requirement is 0.5 ZJ. The challenge now remains to convert a large fraction of the received energy into storable and reusable energy. Many projects using hydrogen as a new energy carrier have emerged in recent years [1-4]. An ecological and almost inexhaustible source of hydrogen atoms is at our disposal: water. It is, therefore, planned to convert and store solar energy in a chemical form (i.e., in binding energies) by splitting water into hydrogen and oxygen through a catalytic process involving a photoactive material. Among the possible processes, photoelectrochemical water splitting can achieve production of hydrogen in a single reactor. This process involves several reaction steps, including the absorption of photons, generation of electron/hole pairs, and the use of these charge carriers in the chemical reactions producing H_2 and O_2 [3]. To utilize photon energies in the visible-light range, it is necessary for the photoresponsive materials to absorb less than 3.1 eV of photon energy, corresponding to the typical bandgap of between 2 and 3 eV [4-5], and to have conduction and valence bands well-positioned relative to the redox potentials for hydrogen and oxygen evolutions.

The material studied in the present contribution is $SrTaO_2N$ (abbreviated as STON hereafter), a perovskite oxynitride compound. $SrTaO_2N$ has an electronic band structure comparable to TaON [6] and $LaTiO_2N$ [7] and, based on its bandgap and band positions, has been identified as a relevant photocatalyst candidate for the water-splitting reactions [8-9]. In our previous study of STON films deposited on Nb:STO substrates [8], we identified the influence of the stoichiometry, namely anion ordering (O/N). Here we aim to generate new insight that will improve our understanding of the physicochemical phenomena responsible for the photoelectrochemical response. This study reports extended experimental data by varying crystallization of films, type of crystallization, impact of different substrates, and thickness of films, and to study their impact on the photoelectrochemical activity of STON thin films. The objective of the study is the determination of intrinsic properties and identification of limiting parameters of STON. In this sense, our study is in line with that of Pichler *et al.* on the photoelectrochemical study of perovskite oxynitride $LaTiO_2N$ films [10]. The present research presents the deposition of three series of STON films by means of reactive radio-frequency (rf) magnetron sputtering (substrate temperature upon deposition, film thickness, and type of substrate), which were varied in order to study their influence on the optoelectronic, structural, and photoelectrochemical properties.

2. Experimental

2.1. Oxynitride STON sputtering target

The sputtering target was made via multi-step processes involving the synthesis of the STON powder and its subsequent shaping as a cylindrical target disc for the deposition of thin films by rf sputtering. For the powder, the first step is to make the $Sr_2Ta_2O_7$ oxide precursor compound by a solid-state chemistry route. Stoichiometric amounts of high purity powders of $SrCO_3$ and Ta_2O_5 were homogenized in isopropanol for 1 h in an agate mortar and dried in an

oven at 110°C. The obtained powder was pressed into a pellet using a uniaxial press, then calcined in air for 15 h at 1000°C, milled, and calcined again at 1400°C for 15 h, and checked for phase identification by X-Ray Diffraction (XRD, PANalytical X'Pert Powder). Once the $Sr_2Ta_2O_7$ compound is synthesized, the powder is placed in a tubular oven under ammonia at 1000°C. The complete nitridation of the powder was conducted through a series of thermal treatments of 40 h each, controlled each time by XRD analysis to check if the STON compound is formed. If the nitrided powder still contains traces of the $Sr_2Ta_2O_7$ oxide phase, it is nitrided for an additional 40 h. To nitride 40 g of powder necessary for the realization of the sputtering target, a total of 370 h of heat treatment has been necessary, as seen in Figure 1 giving the patterns after various nitridation steps. The elemental composition of the final powder was checked by energy dispersive spectroscopy (EDS, Oxford Aztek in a JEOL JSM IT100 SEM): this returned a Sr/Ta ratio of 1.01 and a nitrogen content of 20.5 at.%, which are close to expected values and, thus, confirms the synthesis of the $SrTaO_2N$ compound.

The oxynitride target (75 mm in diameter) was separately made using the STON powder, compacted by uniaxial pressing at 15 tons. No sintering processes were carried out in air due to the susceptibility of oxynitrides to oxidation at moderate and high temperature [11-12]. This limitation has, therefore, made it impossible to use an organic binder to ensure a minimal mechanical strength of the target. The latter is, therefore, very brittle, as shown by the slight cracks observed on the photo shown in Supplementary Figure S1.

2.2. Thin-film deposition

Films were deposited by (Ar + N_2) reactive rf magnetron sputtering (Plassys MP450S) using the prepared STON target. Deposition conditions were the following: rf power P_{RF} = 60 W, total pressure p_T = 13 mTorr, and 25 vol% N_2. Thicknesses were controlled by the sputtering time of the deposition. Three series of samples were deposited: the first series on FTO substrate

(fluorine-doped tin oxide (F:SnO_2) layer on soda-lime glass) by varying the substrate temperature T_S from 300 to 650°C in order to analyze the formation of the oxynitride compound at a moderate temperature; the second series on fused glass (FG) substrate with different thicknesses to analyze the influence of the thickness on the optical, dielectric properties and lifetimes of photo-carriers; and the third series at a fixed substrate temperature (T_S = 800°C) on different type of substrates in order to study the impact of the nature of the substrate (amorphous, single-crystal, metallic) on the properties of the deposited films, especially their crystallization and photoresponse.

Moreover, the tested substrates had specific roles in our study: FTO and FG substrates served for the UV-visible transmittance; the FTO, Nb:STO (niobium-doped Nb:$SrTiO_3$), Au(200 nm)/Ti(10 nm)/FG, and Ta (0.5 mm thick tantalum foil) substrates were employed for the photoelectrochemical study. In that case, a small area of the FTO and Au/Ti/FG substrates were covered by a mask during the deposition in order to maintain a conductive area at the front of the sample for the photo-electrical measurements because, unlike the conductive substrates (Nb:STO, Ta), their backside is not conductive.

2.3. Characterization

X-ray diffraction patterns of films were obtained using a Rigaku SmartLab diffractometer (Cu $K_{\alpha 1}$ radiation). Conventional θ–2θ diagrams were recorded at 0.01° intervals with a 2 s count time at each step. The Lotgering factor (F_L) was used to quantify the film orientation. The Lotgering factor compares the orientation of a film versus a randomly oriented material (i.e., powder) and can vary from 0 for a non-oriented layer to 1 for a fully oriented layer. The Lotgering factor is calculated using the following relations, considering a (00l) orientation of films [13]:

$$F_L = \frac{P_{00l} - P_{0(00l)}}{1 - P_{0(00l)}} \quad \text{with } P_{(00l)} = \frac{\sum I_{(00l)}}{\sum I_{(hkl)}}$$

where (hkl) is used for all families of planes, I(00l) and I(hkl) are the intensities of the (00l) and (hkl) indexed peaks, respectively, and the subscript 0 is relative to the powder reference (JCPDS data).

UV-visible transmittance spectra were recorded using a Perkin-Elmer Lambda 20 spectrometer in the 200–1100 nm wavelengths range. For each sample, the absorption coefficient α is calculated from the transmittance (T) using the relation $\alpha = (1/t)(\ln(1/T))$, where t is the thickness of the film. The bandgap of the material (E_g) is calculated assuming a direct allowed transition and using the relation $(\alpha h\nu)^2 = h\nu - E_g$, where $h\nu$ is the photon energy. In the plot of $(\alpha h\nu)^2$ as a function of $h\nu$, the extrapolation of the linear region of the plot at zero gives the value of E_g [14]. Additional measurements for the determination of the absorption coefficient have been performed using a JASCO J670 spectrophotometer with an integrating sphere that simultaneously measures the transmittance, absorbance and reflectance of the sample.

Energy dispersive spectrometry (EDS) was used to investigate the cations and nitrogen relative compositions of films; analyses were performed using the Aztek OXFORD software through a JEOL JSM IT100 scanning electron microscope (SEM) operating at 10 kV. Surface and cross-section morphologies of films were characterized by the above SEM; the error on the thickness values from the cross-section observations is estimated as being ± 10 nm.

Transient absorption (TA) measurements were performed using the pulse energy of the fundamental output of a Ti:sapphire fs regenerative amplifier operating at 800 nm with 35 fs pulses and a repetition rate of 1 kHz. The pump pulses at 320 nm were created from fs pulses generated in an optical parametric amplifier (TOPAS Prime, Spectra-Physics). To generate the probe pulses (white light), another fraction of the 800 nm amplified pulses was focused onto the 2-mm thick continuously moving CaF_2 crystal. The pump and probe were spatially overlapped on the STON thin film surface after passing through a synchronized mechanical

chopper (500 Hz) that blocked an alternative pump pulse. The transmitted probe pulses were directed to the optical fiber. Depending on the path length of the probe beam, the excited state lifetime of the photoexcited charge carrier was measured to be up to 3.5 ns with respect to the pump pulses. To achieve better signal to noise ratios, the resulting white light was split into two channels named as probe and reference, respectively, and focused on the two different fiber optics. The change in absorption (ΔA) of the excited state is calculated by subtracting absorption of the excited and unexcited sample. ΔA is defined as the following:

$$\Delta A = A_{Pump} - A_{NoPump} = \log(\frac{I_{NoPump}}{I_{Pump}})$$

where A is the absorbance defined by the Beer-Lambert law [$A = \log(I/I_0)$ with $I(t) = I_0.e^{-\alpha.t}$, where I_0 is the incident intensity, I is the intensity of the transmitted probe (without (I_{NoPump}) and with (I_{Pump}) the pump), α is the absorption coefficient and t is the thickness of film]. Spectra were averaged over a time period of 2 s for each time delay, yielding every time-resolved spectrum.

Linear scanning voltammetry (LSV) measurements for the photoelectrochemical characterization were performed on a photoelectrochemical (PEC) system. Three electrodes were used: a working electrode (WE), which is the studied STON film and acts as the anode on which the oxidation of water occurs; a counter-electrode (CE) in platinum that acts as the cathode with the reduction of protons and the production of H_2; and a reference electrode (Ag/AgCl Sat. with KCl) with a standard potential of 0.198 V vs. RHE (reversible hydrogen electrode). A NaOH electrolyte (0.1 M, pH = 13) was used with an Ar bubbling. The measuring cell (Supplementary Figure S2) has a capacity of 100 mL and a flat Pyrex window that allows irradiation. The latter is performed under solar simulator irradiation adjusted to 100 mW cm^{-2} (1 sun). The irradiation is chopped with a mechanical shutter with a frequency of 0.11 Hz (open for 4.5 s, closed for 4.5 s), in order to reveal the influence of irradiation on the sample.

3. Results and Discussion

3.1. Effects of the FTO substrate temperature during sputtering

This series of experiments concerns films deposited on FTO conducting substrate to examine the synthesis of oxynitride films at different substrate temperatures, from 300 to 650°C (the latter is the highest possible temperature on this substrate due to its degradation beyond). The film thicknesses were all around 300 nm. XRD θ–2θ diagrams of the samples are presented in Figure 2. At T_S = 350°C, diffraction peaks for $SrTaO_2N$ (JCPDS 79-1311) are identified and exhibit a polycrystalline growth. It is quite remarkable that T_S as low as 350°C led to the crystallization of the oxynitride phase in contrast to the high synthesis temperatures (~1000°C) generally used for the synthesis of oxynitride powders [15-16]. Figure 2 also shows that the increase of the substrate temperature induces an increase of the $\vec{c}$ axis orientation of films as reflected by the intense (00ℓ) peaks and by the evolution of the Lotgering factor values (Table 1, Supplementary Figure S3).

Figure 3 presents the evolution of the transmittance of films as a function of the wavelength. As can be seen in Table 1, a fall of the bandgap (from 5.30 to 2.50 eV) is observed between the substrate temperatures T_S = 350 and 400°C. Above 400°C (Supplementary Figure S4), bandgaps show a shift towards lower values when the substrate temperature increases. The lowest measured bandgap (2.35 eV) approaches those previously reported on powders (2.1 eV) [17] and thin films (2.27 eV) [18].

Concerning the chemical composition, the Sr/Ta ratios and nitrogen contents of films deposited at various substrate temperatures are given in Table 1, and their evolution as a function of T_S is depicted in Figure 4. It is found that the Sr/Ta ratio decreases as the substrate temperature increases; the ratio Sr/Ta = 1.05 is obtained at T_S = 650°C. Note that the Sr/Ta = 1.00 value can be obtained but at a higher substrate temperature and so, on another substrate (on Ta as seen in Figure 4). For the nitrogen content, except the value obtained at T_S = 300°C

for which the nitrogen content is high (26 at.%), we can assume that all other data are similar and that the observed differences are within the experimental uncertainty of the EDS analysis. The variation of the cationic composition, evidenced here as a function of the deposition temperature, can be explained by the flexibility of the perovskite unit-cell which can account relatively large deviations of the chemical composition compared to the strict stoichiometry. This is in line with the findings of *Rodriguez et al.* [19] who pointed out a perovskite signature in XRD patterns of Sr_xTaO_3 films for strontium contents (x) in the range [0.8-1.2]. A similar feature was also observed by Regnery *et al.* in their study of Sr-Ta-O films [20].

The surface morphologies of the STON films deposited on FTO at different substrate temperatures are shown in Figure 5. A finely granular and very dense structure is seen regardless of the deposition temperature. The roughness associated with a polycrystalline nature seems apparent as the substrate temperature increases. The size of the grains is typically in the range of 100–200 nm.

Overall, using the FTO substrate, the stoichiometry becomes closer to its theoretical stoichiometry at higher Ts, up to 650°C, but at temperatures beyond this, FTO loses its conductivity. At 650°C, the bandgap approached the reported values on the STON material. A summary of the samples characteristics is presented in Table 1.

3.2. Effects of film thickness on FG substrate

This series of experiments uses films deposited on FG substrates, a transparent insulating substrate that can be heated at high temperature for optical measurement purposes. First, two samples were prepared at T_S = 650°C and T_S = 800°C with a film thickness of 300 nm. Results of the EDS analysis (Table 1) show that the Sr/Ta ratio and the nitrogen content of films approach that of the stoichiometric STON compound of when the substrate temperature is increased from T_S = 650°C to 800°C (for the latter, Sr/Ta = 1.03 and at.%N = 20.5). The

XRD patterns of the STON films are ascribed to STON without any impurity phase (Supplementary Figure S5). Maintaining T_S = 800°C, the film thickness was controlled by regulating sputtering time to generate thicknesses of 150 and 600 nm in addition to 300 nm. The UV-visible transmittance, reflectance, and absorbance spectra of the samples as a function of the incident wavelength are presented in Supplementary Figure S6. Figure 6 shows the absorption coefficient α as a function of the wavelength. Comparing the bandgap values of the two samples with a thickness of 300 nm (Supplementary Figure S7), we observe that the film deposited at T_S = 650°C has a slightly larger bandgap (2.39 eV) than that deposited at T_S = 800°C (2.33 eV). The latter value is close to those already reported on the STON thin films [18]. Moreover, we notice that the bandgap slightly decreases with decreasing thickness (Supplementary Figure S8). Concerning the absorption (Figure 6), we observe that the absorption coefficient values of the different samples are in the same range in the visible domain and are slightly lower than 100,000 cm^{-1} at 400 nm. These values are similar to those obtained in one of our previous works on STON films deposited on Nb:STO with different thickness [8]. These values are also comparable to those obtained by Trapalis *et al.* on the Zn_3N_2 nitride material [21]. These values are somewhat lower than those obtained by Ziani *et al.* on Ta_3N_5 thin films, which were in the range 8×10^5 to 1×10^4 cm^{-1} from 300 to 600 nm [22]. Moreover, here for the wavelength value of interest at 585 nm in the next transient absorption measurements, low values close to 3000 cm^{-1} were measured.

Dielectric characteristics of the STON films in the UV-Visible range can be calculated from the above measurements using the relations explained in the reference [22]. Permittivities (Figure 7) shows a fairly large fluctuation as a function of the energy of the incident photon in the range 1 – 3 eV due to interference fringes in the reflectance spectra (Figure S6). In the range 1–3 eV, average permittivities are moderate, between 4.5 and 8, with dielectric loss tangents between 0.2 and 0.7. The highest permittivity is obtained for the 150-nm thin film. These values

are consistent with those obtained in our previous work on STON films deposited on Nb:STO [8] and are comparable to those of Ta_2O_5 showing an optical permittivity of 4.4 [23]. In contrast, Ta_3N_5 films were reported to exhibit a slightly higher permittivity value (17) with lower dielectric losses (0.03) from 10^{14} to 10^{15} Hz [22].

To evaluate the lifetime kinetics of the photo-charge carriers, preliminary measurements of transient absorption (TA) by means of femtosecond pump-probe spectroscopy were performed on the above STON-FG films. TA spectra as a function of time delay from 1 ps to 250 ps in the [420 - 620 nm] range for the 150 nm and 600 nm STON-FG thin films are presented in Figures 8a and 8b. To highlight differences, a comparison of the TA at time delay +1 ps for the two samples is also presented at Figure 8c. Three regions are observed in the transient absorption spectra. The first signal is a ground state bleaching GSB (negative) signal around 450 nm, a second GSB signal at 500 nm, and a broad third signal is an induced absorption (positive TA signal) between 510 to 620 nm.

The first GSB signal at 450 nm is due to the depopulation of the ground state due to bandgap transition and is correlated to the VB free hole dynamics [26]. Both the STON-150 and STON-600 sample present this transition. The kinetics of this transition is rapid; it happens at almost 9 ps (Figure 9a). As a comparison, a career lifetime of a similar material, Ta_3N_5 thin films synthesized by reactive sputtering [22], was measured to be also very short with a career trapping occurring in less than 10 ps. The presence of the second GSB signal at 500 nm can be correlated to the formation of hole trapping nitrogen vacancies (V_N) above the valence band (VB). This process was recently reported on Ta_3N_5 material by Murthy et al. [28] and Ziani et al. [22]. Two bleaching signals were observed at 554 and 590 nm; the first one was assigned to the bandgap transition and the second was assigned to a V_N to CB transition. Here, by correlating the energetic positions of bleaching at 450 nm and 500 nm, we can potentially assign the presence of the GSB signal at 500 nm to the formation of hole trapping V_N states situated

0.27 eV above the VB maximum. Only the STON-600nm presents the two transitions. The STON-150nm looks less defected and presents mainly the bandgap transition. Finally, the broad signal between 510-620 nm can be assigned to be shallowly trapped electrons [28].

Figure 9a depicts the absorbance change evolution as a function of the wavelength for the STON-FG films with different thicknesses. From the variation of ΔA for different time delays, one can determine the amount (i.e., population) of photoelectrons still in the excited states as a function of time (Figure 9b). We can further access the lifetimes of photo-charge carriers. Lifetimes are defined by fitting the curve with a multi-exponential decay function. The fitting of the kinetics of the STON-150nm sample at 550 nm presents three lifetimes of 98 ps (28 % of the total charge carrier population), 3.6 ps (32 %), and less than 1 ps (40 %). The measured lifetimes of the STON-600nm are a combination of 41.2 ps (23 %), 2.4 ps (38 %), and 39 % less than 1 ps. When comparing STON-150nm and STON-600nm, the thin STON-150nm film presents more long-lived holes. Comparing the lifetimes of the STON films to those reported on efficient visible photoactive semiconductors, such as the $BiVO_4$ material [27] with lifetimes as high as 40 ns, one could see that the present lifetimes are low.

As a summary, characteristics of films of this series are presented in Table 1 and underline that the substrate temperature can be further increased beyond T_S = 650°C, up to T_S = 800°C, leading to films very close to the STON stoichiometry. The different thicknesses of the STON films consistently give similar absorption coefficients, while low coefficients of absorption were obtained in the 500–600 nm range; these could represent a first factor explaining the low measured photocurrents on the STON films as seen after. A second factor is also evidenced by TA measurements, the low lifetimes of photo-charge carriers on the order of a few picoseconds to a few tens of picoseconds.

3.3. Effects of the substrate identity

This series of experiments makes use of deposition on different types of substrates, FG, Nb:STO, Au/Ti/FG, and Ta, at T_S = 800°C. Film thicknesses are fixed to be around 300 nm. The film deposited on the FG substrate was the only one measured by UV-visible transmittance because the other substrates (metalized or conductive) are non-transparent; the extracted bandgap is 2.33 eV. Photos of the prepared films are presented in Supplementary Figure S9. XRD measurements of the films were carried out in θ-2θ measurements while keeping the K_β line of copper to obtain higher peak intensities and thus to detect the possible existence of parasitic phases in very small quantities. Bare substrates were also analyzed to locate their diffraction peaks. Patterns of films and substrates are shown in Figure 10.

All deposited films are identified as STON but have different crystalline states, from polycrystalline to totally oriented growth. To quantify the orientation of the films along with their $\vec{c}$ axis, the Lotgering factors (F_L) were calculated (Table 1). The film deposited on the amorphous FG substrate has an F_L = 0.17; this film is polycrystalline, as can also be seen in Figure 10a. Contrarily, the $\{00\ell\}$ family peaks are the only visible peaks for the film deposited on the Nb:STO substrate (Figure 10b), the film is therefore fully $\vec{c}$-oriented with a Lotgering factor of 1. This is explained by the weakest mismatch (m) within this series between the $SrTaO_2N$ material and the Nb:STO single-crystalline substrate (m = + 3.3%); this is the substrate that promotes the best crystal orientation of STON. Several (hkl) peaks are found for the other films deposited on Au/Ti/FG and Ta substrates (Figures 10c and 10d); the films are polycrystalline. Nevertheless, they display a significant degree of $\vec{c}$-axis orientation with F_L = 0.33 and F_L = 0.58 on Au/Ti/FG and Ta, respectively. One can also notice that the peaks are of very low intensity on the Au/Ti/FG substrate, denoting a poor crystallization. For the film deposited on Ta, a fairly intense peak is observed at 2θ ~ 60.6°, which might correspond to the TaN tantalum nitride (JCPDS 49-1283) with a (220) orientation.

By the EDS analysis (Table 1), all Sr/Ta ratios are similar and close to 1, regardless of the substrate; the amount of nitrogen was consistently higher (marginally) than 20 at.%, except for the film on Nb:STO substrate (N = 24.0 at.%).

3.4. Photoelectrochemical measurements on STON films

Photoelectrochemical measurements under visible light were performed by linear sweep voltammetry. As reported by many authors, for instance, Pichler *et al.* in their photoelectrochemical study of $LaTiO_2N$ thin films [10], oxynitride materials undergo a self-oxidation by consuming the created photo-holes. This process, in addition to degrading the photoanode material, produces a photocurrent that adds to the O_2 evolution. As an example, Supplementary Figure S10 presents the first four measurements done on a STON film deposited on Nb:STO substrate deposited at T_S = 800°C. The results show that the photocurrent density was more or less stabilized from the second measurement. Consequently, for the rest of the study, we report the photocurrent density values obtained for the second measurement on each sample.

Supplementary Figure S11 shows the photoresponse of STON films with the same thickness (300 nm) deposited on different substrates (FTO, Nb:STO, Au/Ti/FG and Ta). First, it can be seen that all samples exhibit a photocurrent when irradiated, which confirms that the material responds to visible light. The low photoresponses of the STON-FTO and STON-Au/Ti/FG films can be explained first by their polycrystalline and weak crystallization, respectively, evidenced in the XRD analysis. Photoresponses of the well-crystallized oriented STON-Nb:STO and STON-Ta films are actually higher and demonstrates, as already reported [7], that the crystallinity of films is a key to exhibit a good photoresponse. The photocurrent (19 $\mu A\ cm^{-2}$ at 1 V vs. RHE) measured for the STON-Ta film is consistent with those already reported on similar oxynitride films in the same conditions, in particular in the absence of co-catalysts or electron donor in the reaction medium [7,9,24-25]. For example, Pischler *et al.*

report photocurrent densities close to 10 μA cm^{-2} at 1.5 V vs. RHE for $LaTiO_2N$ films deposited on TiN/MgO substrates [9]. Also, a $LaTiO_2N$ thin film deposited on Nb:STO substrate exhibited a photocurrent density of 5 μA cm^{-2} [7], which was increased by a factor of 16 to 80 μA cm^{-2} when iridium oxide (IrO_2) was deposited on the $LaTiO_2N$ film. Moreover, here, no influence of the cationic composition on the photoresponse can be underlined. On the one hand, the Sr/Ta ratios of the STON films on Nb:STO and Ta are in the range 0.99 – 1.02 and we can assume that they correspond to the stoichiometric value taking into account the EDS uncertainty. On the other hand, only one sample (T_S = 650°C) of the series deposited on FTO (showing a significant variation of the Sr/Ta ratio as a function of the deposition temperature) has been used for the photoelectrochemical experiments. Anyway, for this sample, its weak polycrystalline character is a more prominent factor influencing the photoresponse than any other of its characteristics.

Figure 11 presents the responses of the STON films deposited on Ta substrates with three thicknesses, 150, 300, and 600 nm. The highest photocurrent density is reached on the thickest studied film (600 nm). All the measured films are polycrystalline, with similar Lotgering factors (Table 1) regardless of the thickness, so the observed evolution is not primarily due to the crystallization. From Figure 6, the absorption coefficient showed notable low values in the 400-600 nm range (for example, $\alpha \sim 3000$ cm^{-1} at λ = 585 nm). This could be one of the key factors explaining the low measured photocurrent densities: despite having the proper bandgap (~2.35 eV) for absorption in the visible domain, the STON films exhibit a low absorbance in this range of interest, meaning a non-optimal capture of photons for the photochemical reactions. From this point, the higher photocurrent density obtained for the 600 nm-thick STON film could be explained by the effect of the absorbance that increases with the thickness of films. For higher thicknesses, one can assume a limit for which the recombination of the photoelectrons within the material occurs, resulting in a global reduction of the

photoelectrochemical response. Finally, it is noted that the photoresponses start at more negative than 0 V vs. RHE, suggesting that the conduction band position is located more negative than hydrogen evolution potential, proving that STON is a potential candidate to achieve overall water splitting with a single semiconductor. This result is promising, and performance can likely be further improved by decorating electrocatalyst on its surface.

4. Conclusion

The present study of $SrTaO_2N$ (STON) films deposited by reactive magnetron rf sputtering identified some key optoelectronic characters for O_2-evolving photoanode. Films approach stoichiometry when the substrate temperature increases to T_S = 800°C, with a bandgap of 2.33 eV, a cation ratio Sr/Ta = 1.03, and a nitrogen content of 19.5 at % on FG substrate. However, on FG and Au/Ti/FG, the crystallization of STON is weak with a polycrystalline nature. In contrast, c-axis oriented films are obtained on Ta and Nb:STO substrates. The PEC measurements show a promising very negative onset potential for photoresponse, suggesting that STON is a potential candidate to achieve overall water splitting using a single semiconductor. Three limiting factors can then be highlighted here: a low absorption coefficient, especially in the visible domain from 500 to 600 nm, the short lifetime of photoexcited charge carriers, and the moderate permittivity values (< 10) in the visible domain. Among the deposited $SrTaO_2N$, the highest photoresponse for O_2 evolution under visible light was achieved for the 600 nm-thick sample deposited on Ta because of the dual effects of an oriented growth and a higher absorbance.

Declaration of interests

The authors declare that they have no known competing financial interests or personal relationships that could have appeared to influence the work reported in this paper.

Acknowledgments

This work was supported by the European Union through the European Regional Development Fund (ERDF) and by the Ministry of Higher Education and Research, Brittany Région and Côtes d'Armor Département through the CPER Projects MATECOM and SOPHIE-STICC. This publication work was also supported by the Conseil Départemental des Côtes d'Armor, Saint Brieuc Armor Agglomération, and the Syndicat de Gestion du Pole Universitaire de Saint Brieuc (France). The authors thank Prof. Hicham Idriss and Dr. Habib Katsiev at SABIC corporation for providing the fs pump-probe spectrometer utilities and for the support in the measurements.

References

[1] A. Fujishima, K. Honda, Electrochemical Photolysis of Water at a Semiconductor Electrode, Nature 238 (1972) 37–38. https://doi.org/10.1038/238037a0.

[2] C. N. R. Rao, S. R. Lingampalli, S. Dey, A. Roy, Solar photochemical and thermochemical splitting of water, Phil. Trans. R. Soc. A 374 (2016) 20150088. http://dx.doi.org/10.1098/rsta.2015.0088.

[3] K. Takanabe, Photocatalytic water splitting: quantitative approaches toward photocatalyst by design. ACS Catal. 7 (2017) 8006–8022.https://doi.org/10.1021/acscatal.7b02662.

[4] K. Sivula, R. Krol, Semiconducting materials for photoelectrochemical energy conversion, Nature Reviews Materials 1 (2016) 15010. https://doi.org/10.1038/natrevmats.2016.10.

[5] T. Le Bahers, K. Takanabe, Combined theoretical and experimental characterizations of semiconductors for photoelectrocatalytic applications J. Photochem. Photobiol. C: Photochem. Rev. (2018) in press. https://doi.org/10.1016/j.jphotochemrev.2019.01.001.

[6] M. Xiao, S. Wang, S. Thaweesak, B. Luo, L. Wang, Tantalum (oxy)nitride: narrow bandgap photocatalysts for solar hydrogen generation, Engineering 3 (2017) 365–378. http://dx.doi.org/10.1016/J.ENG.2017.03.019.

[7] C. Le Paven-Thivet, A. Ishikawa, A. Ziani, L. Le Gendre, M. Yoshida, J. Kubota, F. Tessier, K. Domen, Photoelectrochemical properties of crystalline perovskite lanthanum titanium

oxynitride films under visible light. J. Phys. Chem. C 113 (2009) 6156–6162. https://doi.org/10.1021/jp811100r.

[8] A. Ziani, C. Le Paven, L. Le Gendre, F. Marlec, R. Benzerga, F. Tessier, F. Cheviré, M. Hedhili, A. T. Garcia-Esparza, S. Melissen, P. Sautet, T. Le Bahers, K. Takanabe, Photophysical properties of $SrTaO_2N$ thin films and influence of the anion ordering: a joint theoretical and experimental investigation, Chem. Mater. 29 (2017) 3989–3998.https://doi.org/10.1021/acs.chemmater.7b00414.

[9] M. Higashi, R. Abe, T. Takata, K. Domen, Photocatalytic overall water splitting under visible light using $ATaO_2N$ (A = Ca, Sr, Ba) and WO_3 in a IO_3^-/I^- shuttle redox mediated system, Chem. Mater. 21 (2009) 1543–1549.https://doi.org/10.1021/cm803145n.

[10] M. Pichler, W. Si, F. Haydous, H. Tellez, J. Druce, E. Fabbri, M. El Kazzi, M. Dobeli, S. Ninova, U. Aschauer, A. Woaun, D. Pergolesi, T. Lippert, $LaTiO_xN_y$ Thin Film Model Systems for Photocatalytic Water Splitting: Physicochemical Evolution of the Solid–Liquid Interface and the Role of the Crystallographic Orientation, Adv. Funct. Mater. 27 (2017) 1605690. https://doi.org/10.1002/adfm.201605690.

[11] A. Rachel, S. G. Ebbinghaus, M. Güngerich, P. J. Klar, J. Hanss, A. Weidenkaff, A. Reller, Tantalum and niobium perovskite oxynitrides: synthesis and analysis of the thermal behaviour. Thermochimica Acta 438 (2005) 134–143.https://doi.org/10.1016/j.tca.2005.08.010.

[12] R. Aguiar, D. Logvinovich, A. Weidenkaff, A. Reller, S. G. Ebbinghaus, Thermal oxidation of oxynitride perovskites in different atmospheres, Thermochimica Acta 471 (2008) 55–60. https://doi.org/10.1016/j.tca.2008.02.021.

[13] F. K. Lotgering, Topotactical reactions with ferrimagnetic oxides having hexagonal crystal structures, J. Inorg. Nucl. Chem. 9 (1959) 113–123.https://doi.org/10.1016/0022-1902(59)80070-1.

[14] D. Kubelka, L. Munk, Ein beitrag zur optik der farbanstriche, Z. Tech. Phys. 12 (1931) 593–601.

[15] S.-L. Chen, W.-M. Guo, S.-K. Sun, Y. Masubuchi, M. Lv, H.-T. Lin, C.-Y. Wang, Direct synthesis of nearly single phase $SrTaO_2N$ from $SrCO_3$/TaN, Ceram. Int. 44 (2018) 4504–4507. https://doi.org/10.1016/j.ceramint.2017.12.017.

[16] A. Fuertes, Synthetic approaches in oxynitride chemistry, Prog. Solid State Chem. 51 (2018) 63–70.https://doi.org/10.1016/j.progsolidstchem.2017.11.001.

[17] Y. Zhong, Z. Li, X. Zhao, T. Fang, H. Huang, Q. Qian, X. Chang, P. Wang, S. Yan, Z. Yu, Z. Zou, Enhanced water-splitting performance of perovskite $SrTaO_2N$ photoanode film through ameliorating interparticle charge transport, Adv. Funct. Mater. 26 (2016) 7156–7163. https://doi.org/10.1002/adfm.201603021.

[18] D. Oka, Y. Hirose, H. Kamisaka, T. Fukumura, K. Sasa, S. Ishii, H. Matsuzaki, Y. Sato, Y. Ikuhara, T. Hasegawa, Possible ferroelectricity in perovskite oxynitride $SrTaO_2N$ epitaxial thin films, Sci. Reports 4 (2014) 4987.https://doi.org/10.1038/srep04987.

[19] M.A. Rodriguez, T.J. Boyle, B.A. Hernandez, D.R. Tallant, K. Vanheusden, A new metastable thin-film strontium tantalate perovskite, J. Am. Ceram. Soc. 82 (1999) 2101–2105. https://doi.org/10.1111/j.1151-2916.1999.tb02047.x.

[20] S. Regnery, R. Thomas, P. Ehrhart, R. Waser, $SrTa_2O_6$ thin films for high-K dielectric applications grown by chemical vapor deposition on different substrates, J. Appl. Phys. 97 (2005) 073521.https://doi.org/10.1063/1.1873033.

[21] A. Trapalis, J. Heffernan, I. Farrer, J. Sharman, A. Kean, Structural, electrical, and optical characterization of as grown and oxidized zinc nitride thin films. J. Appl. Phys. 120 (2016) 205102.https://doi.org/10.1063/1.4968545.

[22] A. Ziani, E. Nurlaela, D.S. Dhawale, D.A. Silva, E. Alarousu, O.F. Mohammed, K. Takanabe, Carrier dynamics of a visible-light-responsive Ta_3N_5 photoanode for water oxidation, Phys. Chem. Chem. Phys. 17 (2015) 2670-2677.DOI: 10.1039/C4CP05616G.

[23] S. Bécu, Etude des non-linéarités de permittivité de diélectriques utilisés en microélectronique. Application aux capacités MIM. Phd-thesis, Université de Provence - Aix-Marseille I, France, 2006.

[24] N. Nishimura, B. Raphael, K. Maeda, L. Le Gendre, R. Abe, J. Kubota, K. Domen, Effect of TiCl4 treatment on the photoelectrochemical properties of $LaTiO_2N$ electrodes for water splitting under visible light, Thin Solid Films 518 (2010) 5855–5859.https://doi.org/10.1016/j.tsf.2010.05.094.

[25] S. S. Menon, G. Bhalerao, B. Gupta, K. Baskar, S. Singh, Development of $Zn_{1-x-y}Ga_xCo_yO_{1-z}N_z$ as a non-oxide semiconductor material with visible light photoelectrochemical activity, Vacuum 154 (2018) 296–301.https://doi.org/10.1016/j.vacuum.2018.05.023.

[26] P. Maity, O. F. Mohammed, K. Katsiev, H. Idriss, Study of the bulk charge carrier dynamics in anatase and rutile TiO_2 single crystals by femtosecond time-resolved spectroscopy. J. Phys. Chem. C 122 (2018) 8925–8932.https://doi.org/10.1021/acs.jpcc.8b00256.

[27] F. Abdi, T. Savenije, M. May, B. Dam and R. van de Krol, The origin of slow carrier transport in $BiVO_4$ thin film photoanodes: a time-resolved microwave conductivity study, J. Phys. Chem. Lett. 4 (2013) 2752–2757.https://doi.org/10.1021/jz4013257.

[28] D. H. K. Murthy, H. Matsuzaki, Z. Wang, Y. Suzuki, T. Hisatomi, K. Seki, Y. Inoue, K. Domen, A. Furube, Chem. Sci. 10 (2019) 5353-5362.

Figure 1. θ–2θ X-ray diffraction patterns for $Sr_2Ta_2O_7$ powder transformed to $SrTaO_2N$ under nitridation in flowing NH_3 at 1000°C (circled peaks belong to the $Sr_2Ta_2O_7$ phase (JCPDS 72-0921); the top index corresponds to the $SrTaO_2N$ compound (JCPDS 79-1311)).

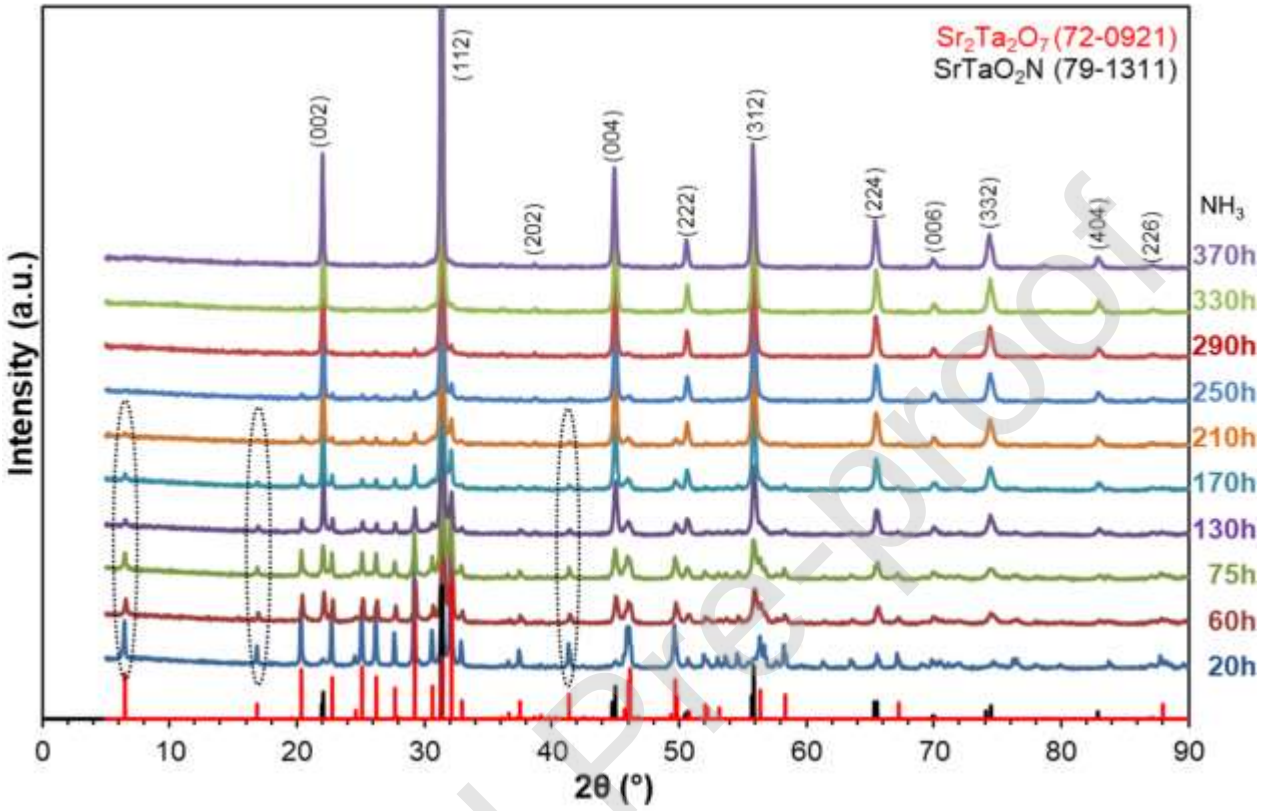

Figure 1. θ–2θ X-ray diffraction patterns for $Sr_2Ta_2O_7$ powder transformed to $SrTaO_2N$ under nitridation in flowing NH_3 at 1000°C (circled peaks belong to the $Sr_2Ta_2O_7$ phase (JCPDS 72-0921); the top index corresponds to the $SrTaO_2N$ compound (JCPDS 79-1311)).

Figure 2. θ–2θ X-ray diffraction patterns of STON films deposited on FTO substrates prepared at different substrate temperatures by reactive rf magnetron sputtering. Indexation is made according to the STON compound. Asterisks indicate are peaks belonging to the FTO/SG substrate.

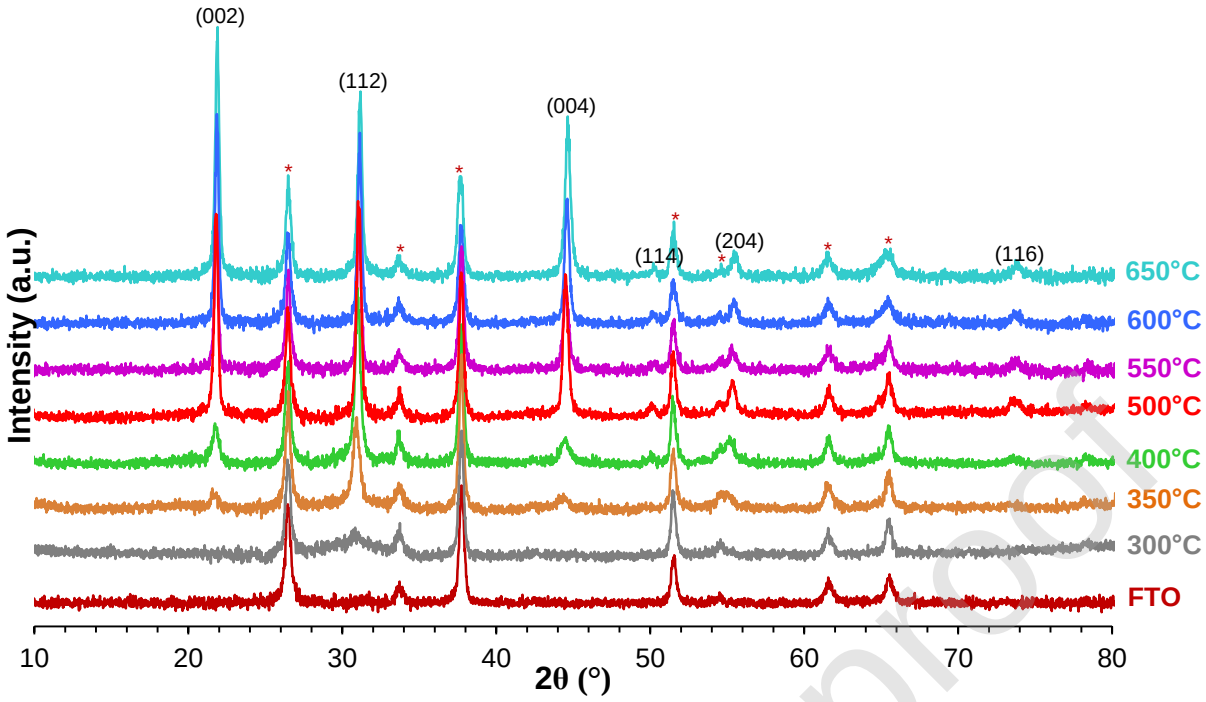

Figure 2. θ–2θ X-ray diffraction patterns of STON films deposited on FTO substrates prepared at different substrate temperatures by reactive rf magnetron sputtering. Indexation is made according to the $SrTaO_2N$ compound. Asterisks indicate peaks belonging to the FTO/SG substrate.

Figure 3. UV-visible transmittance spectra of STON films deposited on FTO substrates at different substrate temperatures by reactive rf magnetron sputtering.

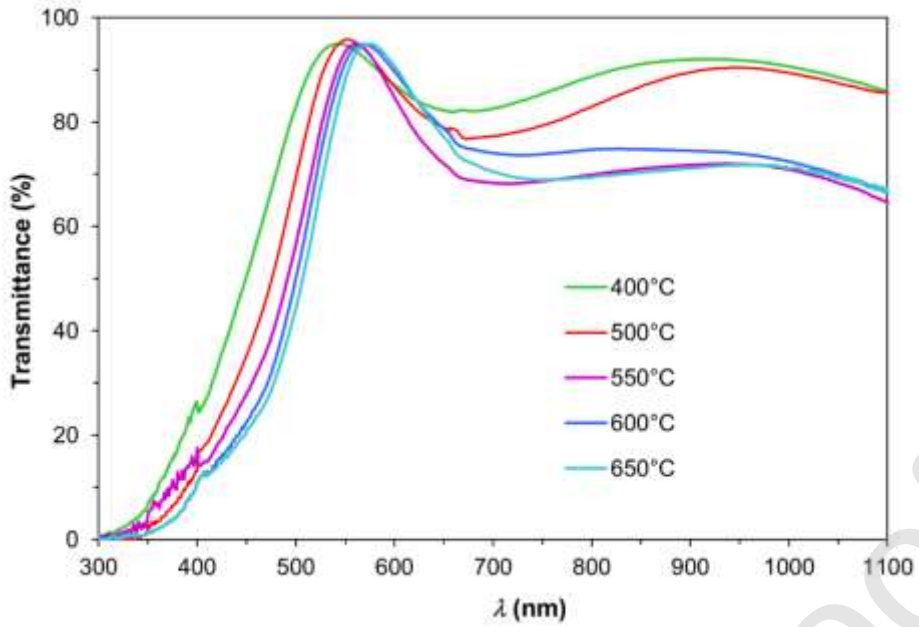

Figure 3. UV-visible transmittance spectra of STON films deposited on FTO substrates at different substrate temperatures by reactive rf magnetron sputtering.

Figure 4. Evolution of the ratio Sr/Ta and the nitrogen content (N at.%) as a function of the substrate temperature for the STON films deposited on FTO substrates prepared by reactive rf magnetron sputtering (as comparison, is given in blue the data for the STON film deposited on Ta substrate at T_S = 800°C).

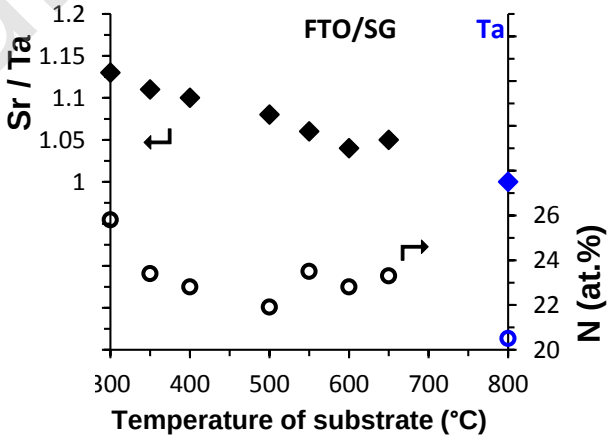

Figure 4. Evolution of the ratio Sr/Ta and the nitrogen content (N at.%) as a function of the substrate temperature for the STON films deposited on FTO substrates prepared by reactive rf magnetron sputtering (as comparison, is given in blue the data for the STON film deposited on Ta substrate at T_S = 800°C).

Figure 5. SEM surface morphologies of STON films deposited on FTO substrates at different substrate temperatures by reactive rf magnetron sputtering (substrate temperature is indicated in the photos).

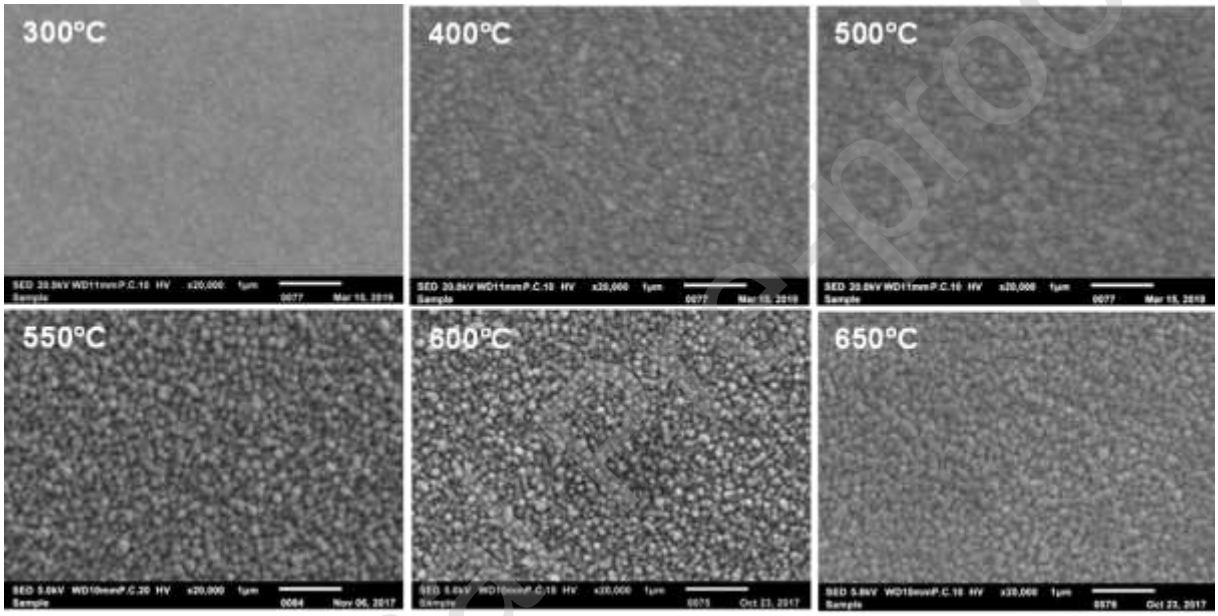

Figure 5. SEM surface morphologies of STON films deposited on FTO substrates at different substrate temperatures by reactive rf magnetron sputtering (substrate temperature is indicated in the photos).

Figure 6. Absorption coefficient of STON films with different thicknesses deposited on FG substrates at T_S = 800°C by reactive rf magnetron sputtering.

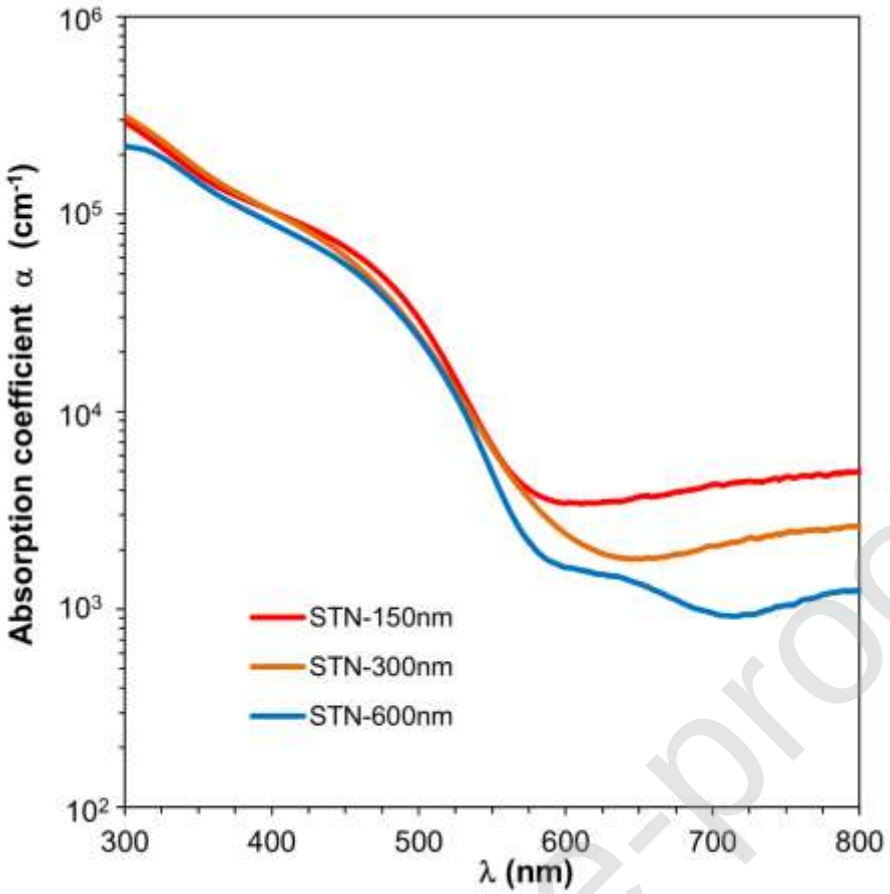

Figure 6. Absorption coefficient of STON films with different thicknesses deposited on FG substrates at T_S = 800°C by reactive rf magnetron sputtering.

Figure 7. Permittivity (ε') and dielectric loss (tanδ) as a function of the photon energy of STON films deposited on FG substrate by reactive rf magnetron sputtering.

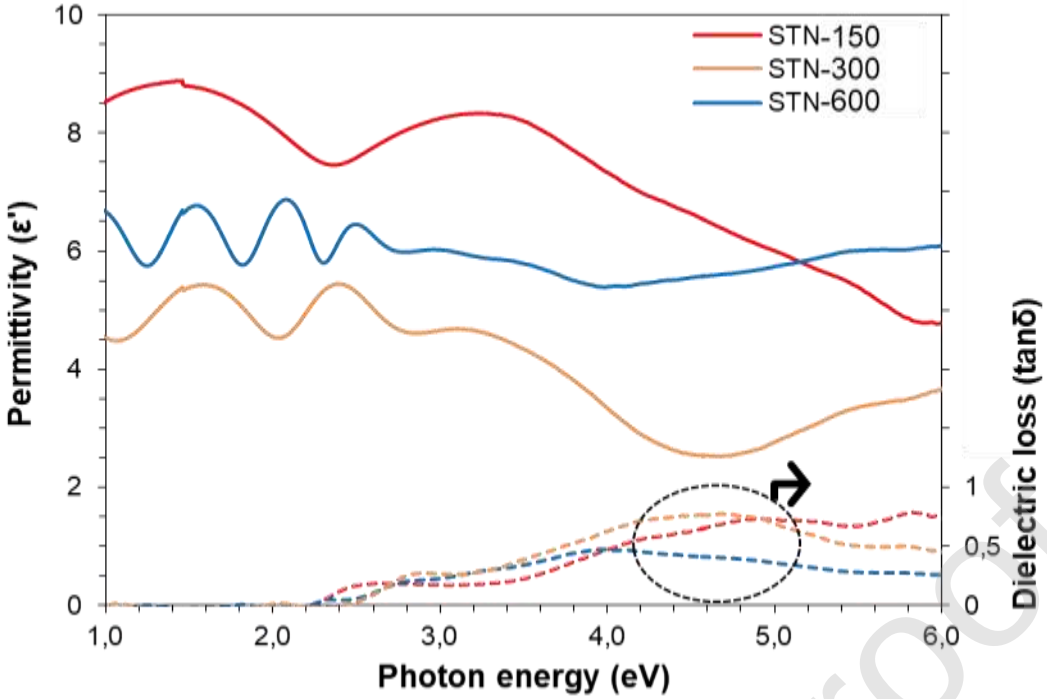

Figure 7. Permittivity (ε') and dielectric loss (tanδ) as a function of the photon energy of STON films deposited on FG substrate by reactive rf magnetron sputtering.

Figure 8. (a) Absorbance change ΔA for an excitation at 330 nm as a function of time delay for the STON-150nm film on FG substrate, and (b) for STON-600nm film deposited on FG substrate. (c) Comparison of the TA of STON-150nm and STON-600nm at time delay +1ps.

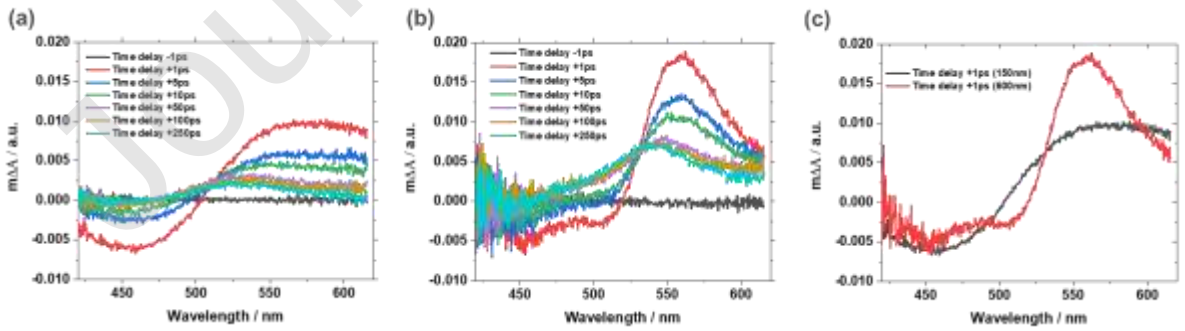

Figure 8. (a) Absorbance change ΔA for an excitation at 330 nm as a function of time delay for the STON-150nm film on FG substrate, and (b) for STON-600nm film deposited on FG substrate. (c) Comparison of the TA of STON-150nm and STON-600nm at time delay +1ps.

Figure 9. (a) Kinetics at 450 nm as a function of the delay and the thickness of STON films deposited on FG substrate and (b) kinetics at 550nm determined by femto pump-probe spectroscopy for an excitation at 330 nm.

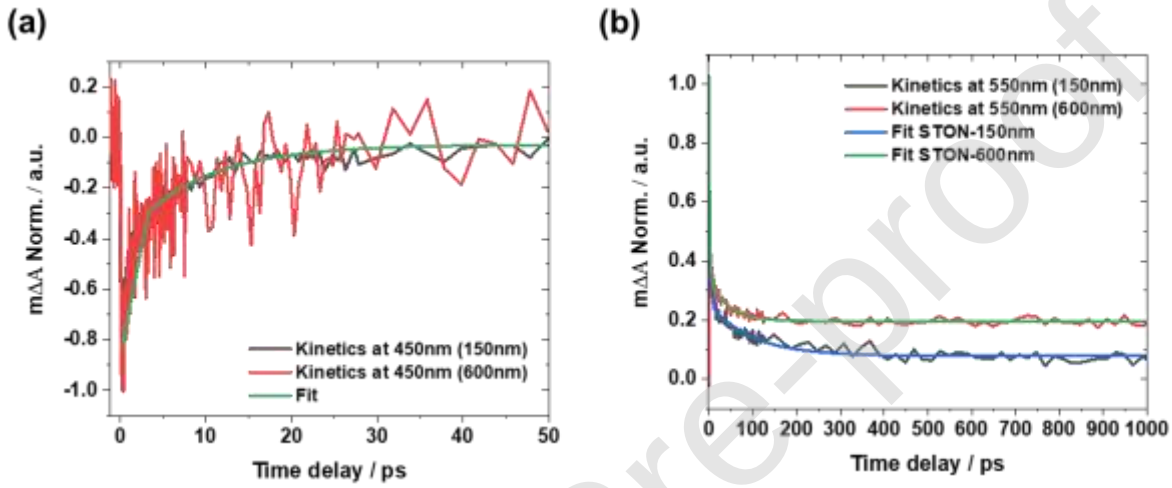

Figure 9. (a) Kinetics at 450 nm as a function of the delay and the thickness of STON films deposited on FG substrate and (b) kinetics at 550nm determined by femto pump-probe spectroscopy for an excitation at 330 nm.

Figure 10. θ–2θ X-ray diffraction patterns of STON films deposited on different types of substrate at T_S = 800°C by reactive rf magnetron sputtering. (a) FG, (b) Nb:$SrTiO_3$, (c) Au/Ti/FG, (d) Ta. The pattern of the bare substrate is shown below each film diagram. Indexation of films is made according to the STON compound. Asterisks indicate peaks belonging to the substrate.

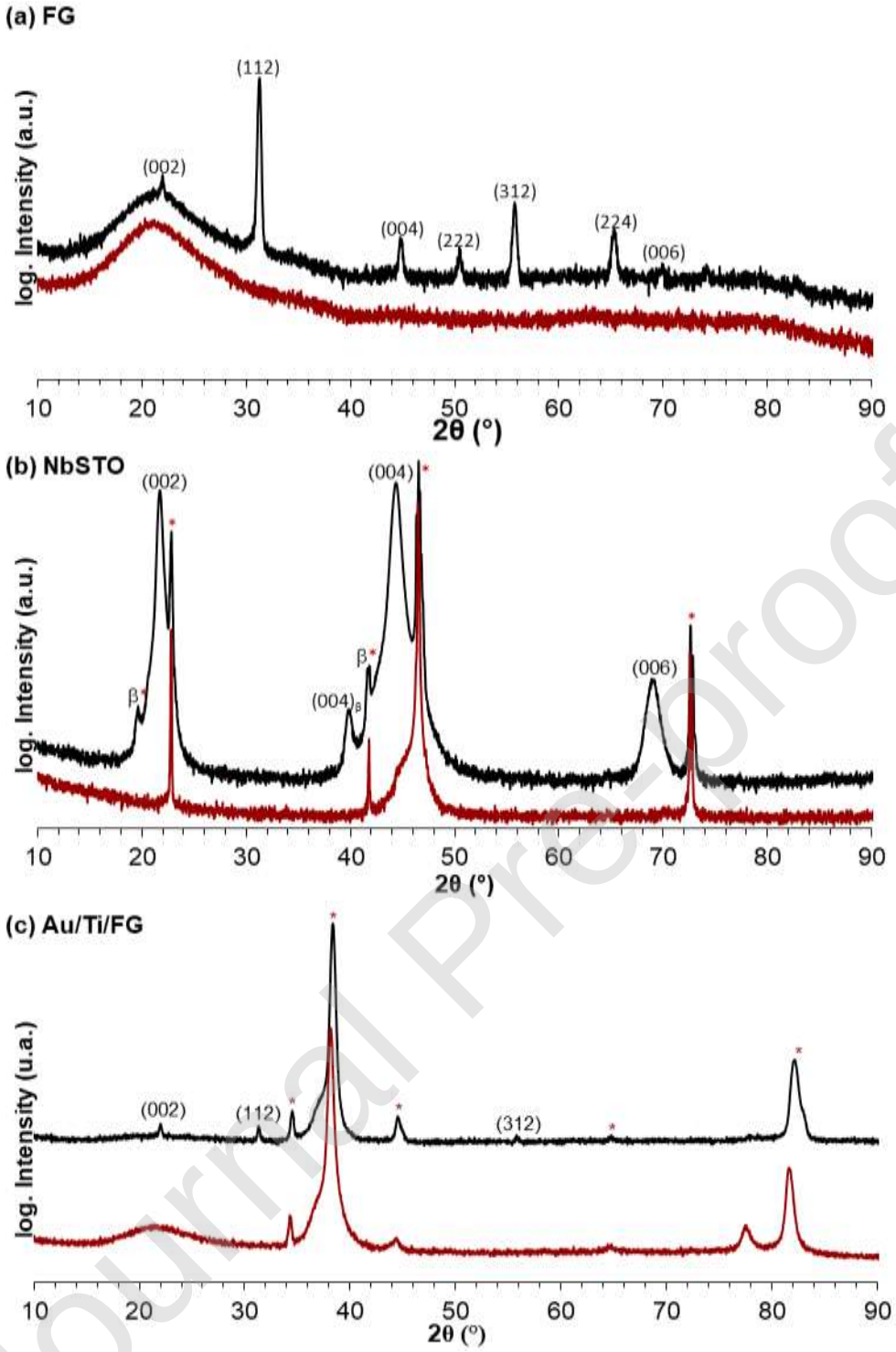

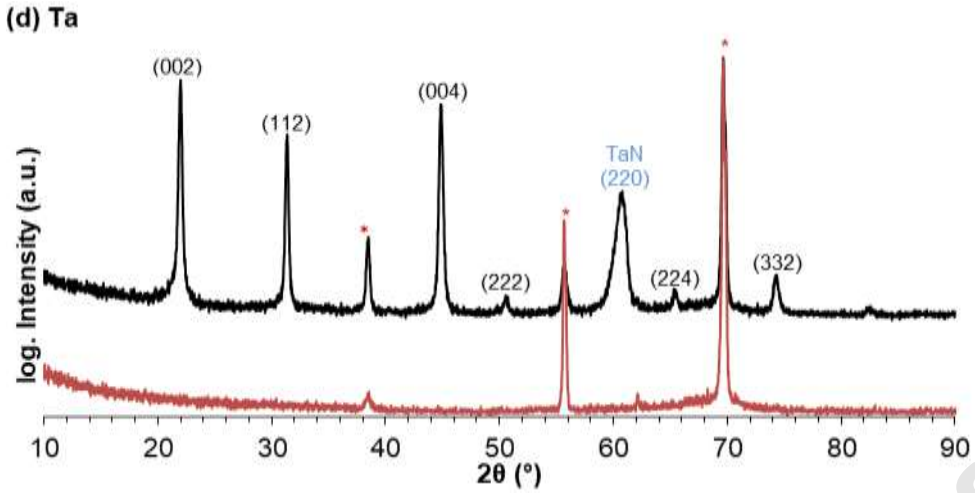

Figure 10. θ–2θ X-ray diffraction patterns of STON films deposited at T_S = 800°C by reactive rf magnetron sputtering on different types of substrate: (a) FG, (b) Nb:$SrTiO_3$, (c) Au/Ti/FG, (d) Ta. The pattern of the bare substrate is shown below each film diagram. Indexation of films is made according to the $SrTaO_2N$ compound. Asterisks indicate peaks belonging to the substrate.

Figure 11. Linear scanning voltammetry measurements of STON films deposited on Ta substrates with different thicknesses. Electrolyte: NaOH (pH 13), Reference Electrode: Ag/AgCl, Counter Electrode: Platinum, Light: 100 mW cm^{-2}.

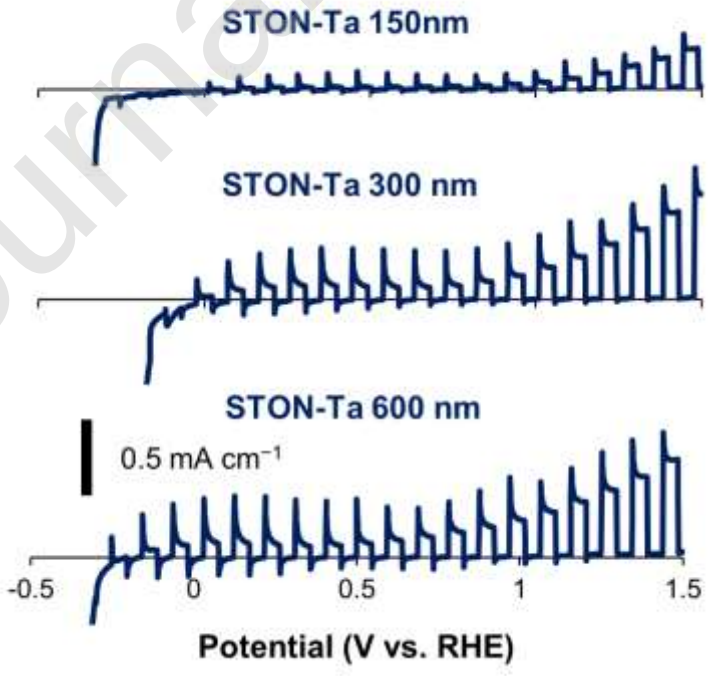

Figure 11. Linear scanning voltammetry measurements of STON films deposited on Ta substrates with different thicknesses. Electrolyte: NaOH (pH 13), Reference Electrode: Ag/AgCl, Counter Electrode: Platinum, Light: 100 mW cm^{-2}.

Table 1. List of STON film properties deposited on various substrates at different substrate temperatures by reactive rf magnetron sputtering.

Substrate	T_S (°C)	Thickness (nm)	Eg (eV)	Sr/Ta	N (at.%)	Lotgering factor F_L	Crystallization
FTO	300	300	5.10	1.13	26.0	/	Amorphous
	350		5.30	1.11	23.5	0.15	Polycrystalline
	400		2.50	1.10	23.0	0.17	Polycrystalline
	500		2.45	1.08	22.0	0.38	Polycrystalline
	550		2.40	1.06	23.5	0.41	Polycrystalline
	600		2.35	1.04	23.0	0.43	Polycrystalline
	650		2.35	1.05	23.5	0.47	Polycrystalline
FG	650	300	2.39	1.19	19.5	0.11	Polycrystalline
	800	150	2.31	-[a]	-[a]	0.23	Polycrystalline
	800	300	2.33	1.03	19.5	0.17	Polycrystalline
	800	600	2.34	0.95	20.5	0.01	Polycrystalline
Nb:STO	800	300	-	1.02	24.0	1.00	Fully textured
Au/Ti/FG	800	300	-	1.01	21.0	0.33	Poorly crystallized
Ta	800	150		-[a]	-[a]	0.44	Polycrystalline
	800	300	-	1.00	20.5	0.58	Polycrystalline
	800	600	-	1.01	20.5	0.57	Polycrystalline